ADVANCED OPTICAL MATERIALS
www.advopticalmat.de

Unveiling Polymorphs and Polytypes of the 2D Layered Semiconducting Gallium Monosulfide

*Yael Gutiérrez, Filippo Agresti, Dilson Juan, Stefano Dicorato, Maria Michela Giangregorio, Fernando Moreno, Pablo García-Fernández, Javier Junquera, Lidia Armelao, and Maria Losurdo**

Polymorphism is gaining attention among van der Waals layered materials. In the case of gallium monosulfide, a hexagonal phase has predominantly been reported. Here the successful growth of rhombohedral gallium sulfide (GaS) with $R\bar{3}m$ space group on sapphire substrates using chemical vapor deposition (CVD) is presented. Crystallographic analysis reveals that the CVD GaS $R\bar{3}m$ has preferred c-axis orientation, low microstrain and moderate mosaicity. A combined approach of X-ray diffraction, Raman spectroscopy and photoluminescence measurements with first principles calculations is used to determine phononic and photonic properties of the rhombohedral GaS with direct band gap of 2.55 eV and near-blue light emission at room temperature. These results pave the way to novel applications in optoelectronics and photonics, particularly for development of efficient light-emitting devices such as LEDs or lasers, quantum dots, photodetectors, and integrated photonic circuits.

1. Introduction

Layered van der Waals (vdW) materials are receiving increasing attention due to their unique optical, electronic, and mechanical properties that are enabling novel applications in several fields spanning from opto-electronics or photonics to photo- and electro-catalysis, to name a few. Among those, transition metal dichalcogenides (TMDs) and their heterostructures have been widely explored.[1,2] Recently, the family of layered post-transition metal chalcogenides (PTMCs), such as indium selenide (InSe[3] In_2Se_3),[4,5] gallium sulfide (GaS),[6–8] gallium selenide (GaSe),[9–12] and gallium telluride (GaTe),[13–15] is gaining interest. In particular, the optical band gap of semiconducting PTMCs varies from 1.5 eV to 3.2 eV, filling the gap-space between semiconducting TMDs and 2D insulators such as hexagonal boron nitride (h-BN) and hafnium sulfide (HfS_2).[16] Specifically, GaS has an optical band gap of 2.5 eV as bulk crystal, that increases up to 3.2 eV for the monolayer.[17] For this reason, it is being exploited in optoelectronic applications including transistors and visible-ultra violet photodetectors,[18–22] photonics,[6] non-linear optics,[23,24] as well as photocatalysis.[8,25]

The layered crystalline structure of semiconducting GaS consists of a stacking along the c-axis of covalently bonded tetralayers (TLs) S-Ga-Ga-S, held together by vdW forces, as shown in **Figure 1**. Each TL is formed by two monoatomic layers of Ga atoms sandwiched between two monoatomic layers of S, with both intralayer metal-chalcogen Ga-S and metal-metal Ga—Ga

Y. Gutiérrez, F. Agresti, M. Losurdo
Istituto di Chimica della Materia Condensata e delle Tecnologie per l'Energia
ICMATE
CNR, C.so Stati Uniti 4, Padova 35127, Italy
E-mail: maria.losurdo@cnr.it

Y. Gutiérrez, D. Juan, F. Moreno
Departamento de Física Aplicada
Universidad de Cantabria
Avenida de los Castros, s/n, Santander 39005, Spain

S. Dicorato, M. M. Giangregorio
Institute of Nanotechnology
CNR-NANOTEC
via Orabona 4, Bari 70126, Italy

P. García-Fernández, J. Junquera
Departamento de Ciencias de la Tierra y Física de la Materia Condensada
Universidad de Cantabria
Avenida de los Castros, s/n, Santander 39005, Spain

L. Armelao
Department of Chemical Sciences
University of Padova
Via Marzolo 1, Padova 35131, Italy

L. Armelao
Department of Chemical Sciences and Materials Technologies (DSCTM)
National Research Council (CNR)
Piazzale A. Moro 7, Roma 00185, Italy

The ORCID identification number(s) for the author(s) of this article can be found under https://doi.org/10.1002/adom.202303002

DOI: 10.1002/adom.202303002

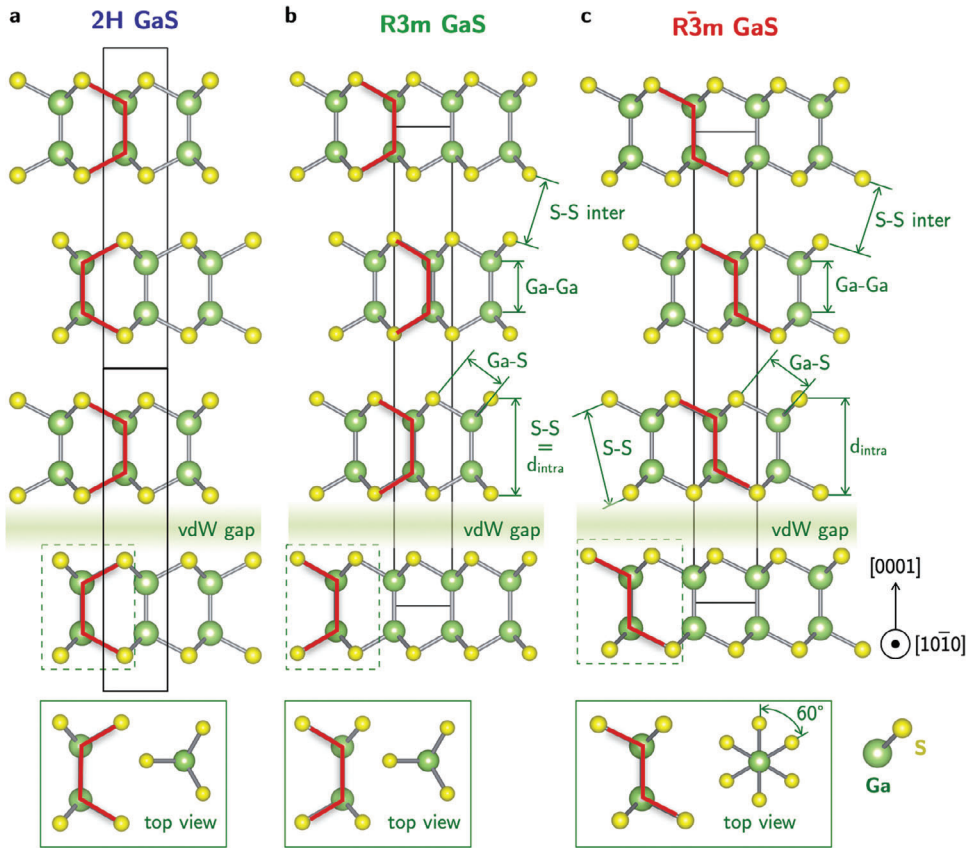

Figure 1. Crystalline structures of a) 2H ($P6_3/mmc$), b) $R3m$ and c) $R\bar{3}m$ GaS. The 2H unit cell has two layers, both the $R3m$ and $R\bar{3}m$ unit cells comprise three layers, hence the label 3R is common. Unit cells [two in panel (a) and one in panels (b) and (c)] are marked with a solid line, reflecting the larger c lattice constant of the 3R GaS. A side and top view sketch of the S-Ga-Ga-S layer and the triple Ga—S bonds for 2H, $R3m$ and $R\bar{3}m$ GaS is shown at the bottom. In the $R\bar{3}m$ GaS, upper S atoms monolayer is rotated by 60° with respect to the lower one. Arrows indicate the bond distances reported in Table 1. The red lines are plotted as a reference of the orientation and symmetry of the layers in each crystalline structure.

bonds, differently from most known TMDs such as molybdenum disulfide (MoS_2). The weak vdW interaction between TLs has been reported to allow the formation of different polymorphs and stacking polytypes in TMDs and PMTCs.[26] Most commonly encountered polymorphs in TMDs are 1T (trigonal), 2H (hexagonal) and 3R (rhombohedral), with the number indicating the X–M–X units in the unit cell (that is, the number of layers in the stacking sequence). The 2H phase is reported to be the most thermodynamically stable phase, while the 1T phase and 3R phases are metastable and revert to the 2H phase over time, or upon application of some form of energy that allows them to overcome the associated activation barrier.[27,28]

Polymorphs are relevant as the change in the crystal structure is reflected in a transformation of the electronic structure of 2D materials leading to strong modifications in their properties. A recent example of phase transitions between polymorphs in 2D TMD is the semiconducting 2H to metallic 1T phase transition in few layers MoS_2[29,30] and $MoTe_2$.[31]

In the case of gallium monochalcogenides, such as gallium selenide (GaSe), the existence of several polytypes, i.e., $\beta-$, $\epsilon-$, $\delta-$ and $\gamma-$ GaSe, has been reported, and a new stable polymorph ($\gamma'-$ GaSe) has been very recently discovered.[26,32,33] Conversely, in the case of GaS, the stable 2H GaS or $\beta-$ GaS phase has mainly been studied and reported in literature [7,8,23,25,34]. Only two studies mention a rhombohedral 3R phase of GaS and never proven to be stable.[24,35,36]

In this work, we demonstrate the successful growth of 3R GaS thin films using chemical vapour deposition (CVD). We present the structural, phononic and electronic properties of 3R GaS, studied both experimentally and theoretically through first principles calculations. By integrating experimental techniques such as photoluminescence, Raman spectroscopy, and X-ray diffraction measurements with density functional theory (DFT) calculations, we successfully identified the 3R phase as belonging to the space group $R\bar{3}m$. Differently from the indirect bandgap 2H-GaS, the $R\bar{3}m$ GaS has direct band gap of 2.55 eV and near-blue light emission at room temperature.

2. 2H versus 3R Crystalline Structures

Figure 1a shows the crystalline structure of 2H GaS, which is the most commonly reported phase of GaS. It crystallizes in a hexagonal lattice with space group $P6_3/mmc$ (no. 194), with lattice parameters $a = 3.587$ Å and $c = 15.492$ Å.[37] Each layer is non-centrosymmetric, and the layers are stacked following alternating rotations of 180° around the c-axis. In each S-Ga-Ga-S layer, Ga atoms sit on top of each other and the S atoms are also aligned. The 2H phase has AB stacking order of adjacent

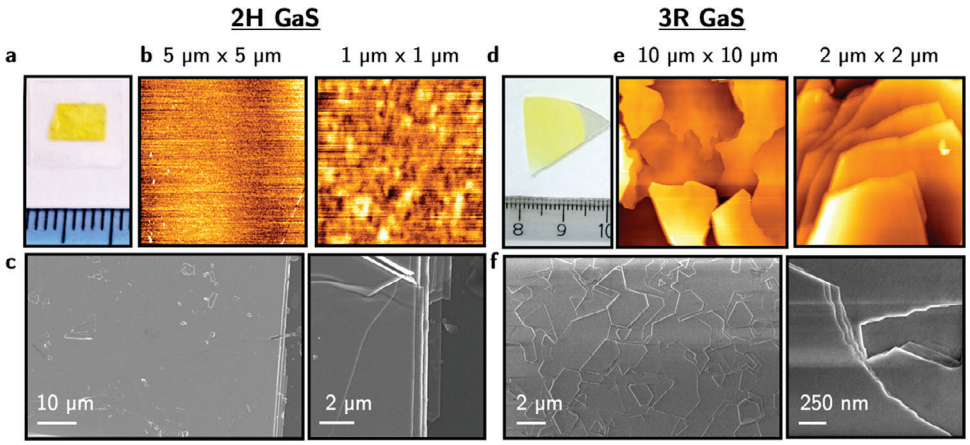

Figure 2. a) Picture with reference size-scale, b) AFM topography and c) SEM images of 2H GaS reference sample. d) Picture with reference size-scale, e) AFM topography and f) SEM images of the cm-scale size 3R CVD grown sample. The layered structure of both the 2H GaS and 3R GaS is visible at the edges, where layers can be counted.

layers in opposite crystalline orientation, leading to centrosymmetry (non-centrosymmetry) in even (odd) numbered layers. Figure 1b shows an additional GaS polytype, and Figure 1c another polymorph of the 2H phase, each of them with rhombohedral symmetry. Therefore, the corresponding space groups are $R3m$ (space group no. 160) for the polytype of Figure 1b, and $R\bar{3}m$ (space group no. 166) for the polymorph of Figure 1c. In the scarce literature on the rhombohedral phase of GaS, the final determination of the space group between $R\bar{3}m$ and $R3m$ is still an open question [24,35,36]. The layer in $R3m$ GaS is non-centrosymmetric with a horizontal mirror plane perpendicular to the *c*-axis, preserving the same symmetry of the 2H phase (see Figure 1b). Differently, in $R3m$ phase the layers are stacked along the *c*-axis with no alternating rotation but translated 1/3 of the unit cell along the [1010] direction. Conversely, the crystalline structure of the $R\bar{3}m$ GaS polymorph, as seen in Figure 1c, also has the layers stacked with a displacement of 1/3 of unit cell along the [1010] direction, with Ga atoms sitting on top of each other in each layer, but with the S atoms of the bottom layer rotated 60° with respect to the S atoms of the top layer within each layer, as can be seen in the top view at the bottom of Figure 1c. Therefore, for $R\bar{3}m$ GaS, both the layer and the crystal unit cell are centrosymmetric. The 3R polytype with space group $R3m$ has AA stacking order with a slight in-plane shift. Zhao et al.[38] reported that the 3R phase of MoS_2, with the same space group $R3m$ and AA stacking order, presents parallel in-plane dipoles in the non-linear regime due to the absence of inversion symmetry. Hence, it possesses effective second-order susceptibility ($\chi 2$) and phase-matched second harmonic generation (SHG) from monolayer to bulk crystal regardless of the number of layers. In this regard, synthesis and further research of the GaS $R3m$ polytype could be interesting for applications in non-linear optics.

3. Results

3.1. Imaging and X-Ray Diffraction Structural Analysis

Figures 2a,d show pictures of a reference 2H GaS sample [39] (exfoliated from a bulk crystal grown with the Bridgman method), and of a cm-scale size 3R CVD sample grown on *c*-sapphire substrate. Atomic force microscopy (AFM) topography images in Figure 1b, representing the 2H GaS sample, reveal a smooth surface with a root-mean-square surface roughness (RMS) of 0.20 ± 0.02 nm. This is corroborated by the scanning electron microscopy (SEM) images in Figure 1c, which show that the film exhibits a uniform surface, with the layered structure evident at the film edges. Noteworthy, the 3R GaS CVD sample has also a layered morphology as shown in the AFM and SEM images in **Figure 2**d,f. Semi-quantitative chemical analysis performed by X-ray photoelectron spectroscopy (XPS) of both the reference 2H and the 3R CVD GaS samples, confirmed the GaS stoichiometry with S:Ga ratios of 1.10 ± 0.05 and 1.05 ± 0.05, respectively.

Figure 3a shows a classical Bragg-Brentano diffraction profile of the 3R CVD GaS film compared to that of a 2H GaS reference crystal. The calculated (tabulated) intensities and positions of [00l] oriented 2H and 3R structures are also reported for comparison. No other peaks from any secondary phases can be observed. The details of the reflection positions are given in the table, from which, it is evident the difficulty in establishing unambiguously the 2H or 3R polymorphs only by a classical Bragg-Brentano scan. Therefore, to investigate further the crystal structure of the CVD grown GaS film, reciprocal space mapping X-ray diffraction (XRD) was performed covering the full reciprocal space available to the diffractometer in the grazing incidence geometry. Figure 3b shows the comparison between experimental reflection positions obtained at low resolution by spinning the sample around the ϕ axis, superimposed to those calculated for 2H and 3R GaS phases. Figure 3c reports the main spots that have been obtained at higher resolution in order to calculate structural parameters. All the experimental reflections can be assigned to the 3R GaS. The analysis of higher resolution reflections of GaS (009) (Figure 3d) and GaS (0117) (Figure 3e) show, respectively, a modest elongation of the reflections along the normal direction to the line connecting the spot and the origin of reciprocal space, which is an indication of a moderate mosaicity, with a distribution around the [001] direction. The mosaic spread and the lateral correlation length, which is the lateral size of the mosaic blocks, have been evaluated from the inclination and elongation

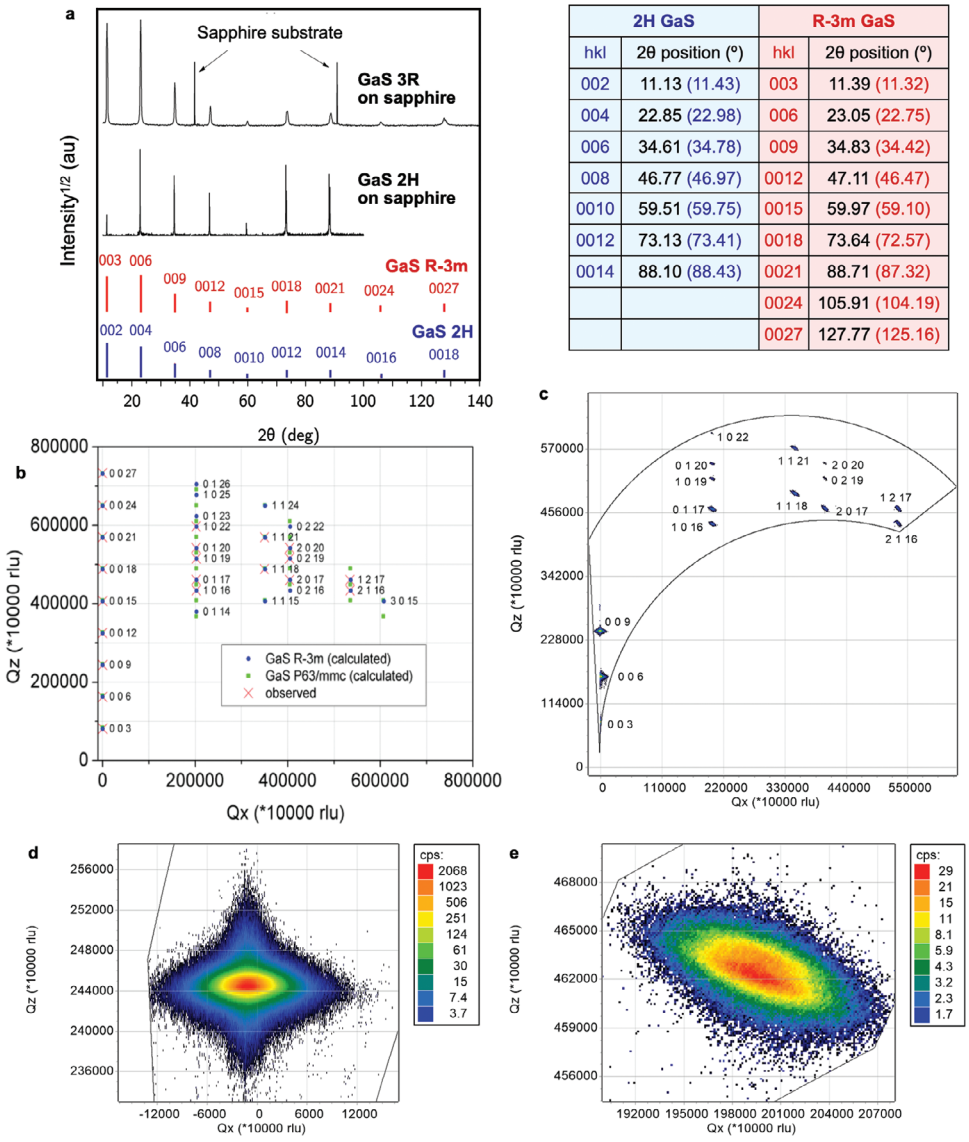

2H GaS		R-3m GaS	
hkl	2θ position (°)	hkl	2θ position (°)
002	11.13 (11.43)	003	11.39 (11.32)
004	22.85 (22.98)	006	23.05 (22.75)
006	34.61 (34.78)	009	34.83 (34.42)
008	46.77 (46.97)	0012	47.11 (46.47)
0010	59.51 (59.75)	0015	59.97 (59.10)
0012	73.13 (73.41)	0018	73.64 (72.57)
0014	88.10 (88.43)	0021	88.71 (87.32)
		0024	105.91 (104.19)
		0027	127.77 (125.16)

Figure 3. a) Classical Bragg-Brentano diffraction profile showing a comparison between the 3R GaS film grown in this work and a reference 2H GaS crystal. Both are [001] oriented. Calculated positions and intensities for 2H and 3R are also shown. b) Comparison between experimentally measured and tabulated positions in reciprocal space map for 2H and 3R GaS. c) Reciprocal space mapping (RSM) of high-resolution reflections obtained in the reciprocal space available for the diffractometer at grazing angle geometry. Indexing refers to 3R structure. d) Reciprocal space map of GaS (009). e) Reciprocal space map of GaS (0117).

of several asymmetric diffraction spots in the reciprocal space, following the procedure described by Fewster.[40] The main contribution to spots shape comes from the mosaic spread with an estimated value of (0.5±0.1)°, while the contribution from the lateral correlation length is almost negligible and it is only possible to state a value of at least 800 nm, which is actually compatible with the pictures shown in Figure 2. The (009) spot is quite narrow and symmetric in the Q_z direction indicating a low microstrain (point defects) and the absence of evident cell parameter *c* relaxations along the film thickness. No signs of relaxation are also visible for asymmetric spots that are also influenced by cell parameter *a*. The root mean square (r.m.s) microstrain has been evaluated from the broadening of peaks shown in Figure 3a by Rietveld refinement; the estimated value is $(1.5\pm0.1)\cdot10^{-3}$. The intensities of asymmetric reflections are quasi-constant by rotating the sample around the ϕ axis, revealing that the islands have random orientations around the [00l] direction.

Our experimentally determined lattice parameters, interatomic distances of nearest neighbors and characteristic angles between atoms are shown in **Table 1** along with the values obtained by Kuhn et al.,[37] for the 2H phase and by Pardo et al.,[35] for the 3R phase (it is worth noting that the authors in Ref. [30] find the best agreement between their XRD data and the theoretical model with $R\bar{3}m$ symmetry). Experimental measurements are complemented by DFT calculations of equilibrium structural parameters for the 2H, $R3m$ and $R\bar{3}m$ phases. We find an excellent agreement between our experimental measures and those reported in literature for the 2H GaS phase. The theoretical

Table 1. Comparison of the hexagonal cell parameters (*a* and *c*), interatomic distances and angles between S-GaS and S-Ga-Ga obtained experimentally and by DFT calculation for 2H and 3R GaS. Data from Pardo et al.[35] and from Kuhn et al.[37] are also reported for comparison. The interatomic distances shown in this table are indicated in Figure 1. Distances are in Å and angles in sexagesimal degrees labeled by the three defining atoms.

	a	*c*	Ga-Ga	Ga-S	S-S	d_{intra}	S-S_{inter}	S-Ga-S	S-Ga-Ga	
Exp.	3.587	15.504	2.439	2.334	–	4.615	3.753	100.15	117.82	2H
DFT	3.584	15.455	2.435	2.339	–	4.618	3.735	99.99	117.81	
Reference[37]	3.587	15.492	2.447	2.334	–	4.599	3.768	100.46	117.44	
Exp.	3.594	23.174	2.507	2.325	5.050	4.604	3.748	101.25	116.82	$R\bar{3}m$
DFT	3.594	23.074	2.431	2.342	5.050	4.604	3.720	100.21	117.64	
Reference[35]	3.605	23.450	2.472	2.347	5.085	4.640	3.798	100.36	117.52	
DFT	3.586	23.063	2.435	2.339	5.050	4.616	3.705	100.06	117.76	*R*3*m*
Reference[35]	3.605	23.450	2.472	2.347	–	4.641	3.797	100.35	117.52	

in-plane lattice parameter *a* has a 0.1% deviation from the experimental value, whereas the out-of-plane lattice parameter *c* is only 0.25% smaller.

Differences in interatomic distances and angles are less than 0.9%. Therefore, the good agreement for the widely studied 2H phase validates our first principles description. From our XRD data, a structural model of the $R\bar{3}m$ crystallographic phase has been constructed and the lattice parameters obtained are also reported on Table 1. The DFT values agree closely with our experimental values for both the in- and out-of-plane directions.

3.2. Raman Spectroscopy and Phonon Structure

Figure 4a shows the statistical distribution of the Raman spectra measured over more than 10 CVD samples of both 2H and 3R GaS; additionally, within each sample, several measurements were taken in various random points in order to check the homogeneity. Specifically, Figure 4a compares the Raman spectra of CVD grown single phase 3R and 2H samples, as well as that of CVD mixed (2H+3R) samples. As reference, the Raman spectra measured for an exfoliated 2H GaS single crystal is also shown.

The colored shadowed region in the spectra indicates the standard deviation of the relative amplitude of the modes whereas the solid line represents the mean value. The vertical lines at the bottom of the figure indicate the frequencies of the Raman modes in 2H, $R\bar{3}m$ and *R*3*m* GaS calculated by density functional perturbation theory (DFPT). These calculated frequencies, as well as those experimentally measured for the 2H and 3R GaS, are presented in the **Table 2**. An scheme of the vibrations in the lattice corresponding to each mode are shown in Figure 4g. The main active Raman modes of 2H GaS, as determined by the irreducible representation of the point group D_{6h}, are the A_{1g}, E_{1g} and E_{2g}, and appear in the experimental Raman spectrum at frequencies of 76 (E_{1g}), 188 (A_{1g}), 298 (E_{2g}), and 363 cm^{-1} (A_{1g}). The position of the Raman modes agrees well with the spectral peaks attributed to GaS reported in Refs.[41–44] and DFPT calculations shown in Table 2. In the backscattering configuration used here, the E_{1g} mode is forbidden. However, the appearance of forbidden Raman modes of layered materials has been recently reported to be selectively detected at the edge regions of the layers. The distorted polarization of the electromagnetic fields at the layered material/air interfaces breaks the symmetry, making forbidden Raman modes visible.[45] Interestingly, for the 2H GaS single crystals, an intensity ratio between A_{1g} modes of 1.0 ± 0.1 has been reported. This ratio indicates that the grown GaS single crystal has a single phase, good crystalline quality, and well-defined crystal axes.

In the case of the $R\bar{3}m$ GaS (point group D_{3d}), equivalent Raman modes in the studied range are A_{1g} and E_g, with calculated frequencies of 71.6 (E_g), 182.3 (A_{1g}), 278.9 (E_g) and 355.5 cm^{-1} (A_{1g}). For *R*3*m* GaS (point group C_{3v}), the main Raman modes are A_1, E(TO) and E(LO), with calculated frequencies of 88.0 [E(TO)], 181.3 (A_1), 280.92 [E(TO)], 281.03 [E(LO)], 288.06 [E(TO)], 313.25 [E(LO)] and 355.9 cm^{-1} (A_1).

The main differences in the experimental Raman spectra of the 2H and 3R GaS are in the E symmetry mode. Specifically, Figure 4b shows the comparison of the CVD 2H, 3R and 2H+3R GaS Raman spectra in the 275 – 305 cm^{-1} range as compared to the 2H single crystal. The peak for the 2H, both CVD and single crystal, is asymmetric, and it can be deconvoluted into two components, one very weak at 290 cm^{-1} and a stronger one at 295 cm^{-1} assigned to E_{1g} and E_{2g} modes. Conversely, the peak of 3R GaS has a symmetric gaussian shape with only one component due to the E_g mode. In the case of the 2H+3R mixed phase, the peak appears at 292.5 cm^{-1} and can be deconvoluted into two components of equal amplitude located at 290 (3R) and 295 (2H) cm^{-1}. The scanning electron images reported in Figure 4c–e also show the different morphologies of the 2H, 3R and 2H+3R mixed CVD GaS films.

Noteworthy, there is a measurable shift between E modes of 2H and 3R GaS of 5 ± 1 cm^{-1} [i.e., E(2H) at 295 cm^{-1} and E(3R) at 290 cm^{-1}]. This shift is compatible with those calculated from the DFPT calculations, shown in Table 2. For the $R\bar{3}m$ phase, the calculated shift is 6.4 cm^{-1}. In the case of the *R*3*m*, the shift is 4.4 cm^{-1} calculated from the E(TO) mode at 280.92 cm^{-1} (the E(TO) mode at 288.06 cm^{-1} shown in Figure 4a is predicted to have two orders of magnitude lower intensity and, therefore, has not been considered in this comparison). Hence, the shift of the E symmetry mode at around 290 cm^{-1} is an indicator of the presence of 3R GaS and could distinguish between the 2H and 3R phases; however, it does not allow to distinguish between the $R\bar{3}m$ and *R*3*m* symmetries. An indicator to distinguish between these space groups could be the position of the Raman E-mode below 100 cm^{-1}. Theoretical calculated spectral position of equivalent E modes in 2H and $R\bar{3}m$ phase reveals very close values

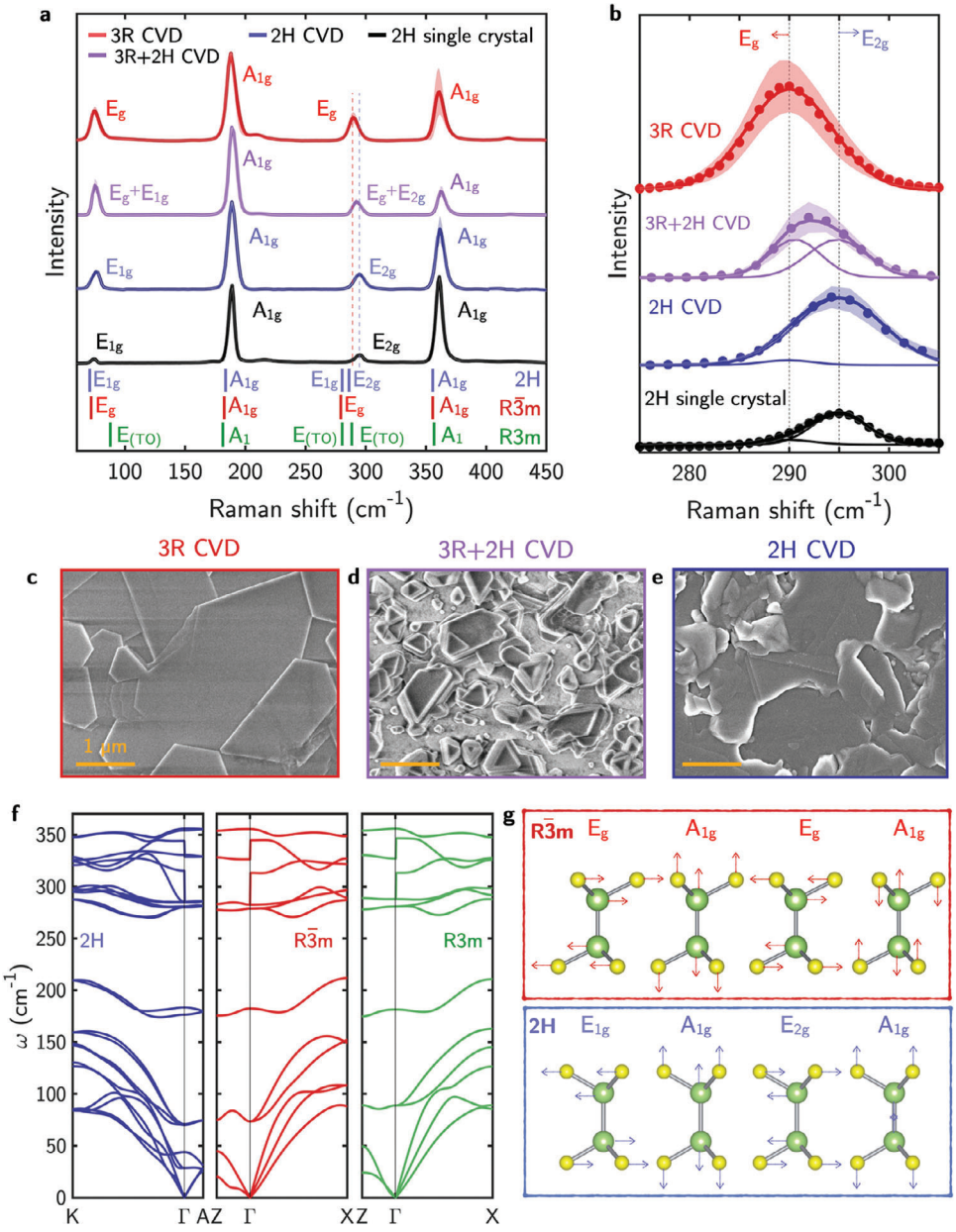

Figure 4. a) Experimental Raman spectra of 3R, 2H, and 2H+3R CVD GaS films grown on *c*-sapphire as compared to that of 2H single crystal GaS. The green probing laser of 532 nm has energy below the GaS bandgap where the absorption coefficient is almost null. Consequently the laser is probing the whole film thickness in all cases. The DFPT calculated Raman modes positions of 2H, $R\bar{3}m$ and $R3m$ GaS are also plotted as reference. b) Zoomed plot of experimentally measured high frequency E Raman mode in 3R, 2H and mixed 2H+3R CVD GaS, highlighting the shift in peak position. The value of the 2H single crystal is shown as reference. SEM images indicating the different morphologies of the c) 3R, d) mixed 2H+3R and (e) 3R CVD grown GaS films. f) Phonon band structure of 2H, $R\bar{3}m$, and $R3m$ GaS, calculated through DFPT, around the Γ point for two high symmetry directions in the corresponding Brillouin zone (BZ). g) Schematic illustration of the atom vibrations for the experimentally observed Raman modes in 2H and $R\bar{3}m$ GaS.

of 70.05 and 71.65 cm^{-1}, respectively. On the contrary, for the $R3m$ GaS, the calculated E mode is at 88.00 cm^{-1}, significantly shifted with respect to that of the 2H GaS, making this result incompatible with the experimental measurements, as the experimentally measured low frequency E modes for 2H and 3R GaS have matching positions. Therefore, this comparison between experimental measures and theoretical calculations of the position of the Raman modes supports the hypothesis of the $R\bar{3}m$ phase space group.

The calculated phonon dispersion of each system is shown in Figure 4f near the Γ point. The crossing of the bands at the Γ point correspond to the frequency of the Raman modes. For 2H GaS, we employed an eight atoms unit cell giving 3 acoustic branches and 21 optic branches, whereas for rhombohedral

Table 2. Experimental and calculated frequencies of the main Raman modes in 2H and 3R GaS, along with reference values from literature. The calculated shifts (ΔE_{2H}) of the high frequency E modes of $R\bar{3}m$ and $R3m$ GaS with respect to that of 2H GaS are also reported in the last column. Calculations done within DFPT approach.

	E mode [cm^{-1}]			A mode [cm^{-1}]			E mode [cm^{-1}]			A mode [cm^{-1}]			ΔE_{2H} [cm^{-1}]	
	2H	$R\bar{3}m$	$R3m$	2H	$R\bar{3}m$	$R3m$	2H	$R\bar{3}m$	$R3m$	2H	$R\bar{3}m$	$R3m$	$R\bar{3}m$	$R3m$
Exp.	76 ± 1	76 ± 1		188 ± 1	188 ± 1		295 ± 1	290 ± 1		363 ± 1	362 ± 1		5 ± 2	
DFPT	70.1	71.6	88.0	183.4	182.3	181.3	285.3	278.9	280.9	355.9	355.5	355.9	6.4	4.4
Reference[37]	75	–	–	189	–	–	292	–	–	360	–	–	–	–
Reference[37]	74	–	–	188	–	–	295	–	–	360	–	–	–	–

symmetries we employed primitive four atom unit cells that display only 9 optical branches. Broad features are common to the three structures, showing clustering of bands at different frequencies given by the nature of the vibrations and a phononic band gap of ≈ 60 cm^{-1}. Notably, a phononic band gap has been recently investigated in related IV-VI monocalchogenides compounds and thermoelectric applications are surmised.[46] The acoustic phonons are comprised of a pair of transverse and longitudinal branches for in-plane vibrations, and a flexural branch for out-of-plane modes. Highest frequency modes reach 360 cm^{-1} approximately.

3.3. Total Energy Calculations

In order to have a better insight into the phase stability, we calculated the electronic energy (U_{el}), the vibrational energy (U_{ph}), the entropy (S_{ph}) and the Helmholtz free energy (F) of the 3R and 2H GaS phases. Particularly, DFT-based packages as Quantum Espresso (QE)[47] calculate the entropy and the Helmholtz free energy considering only the phonon contributions. Therefore, the relationship $F = U_{ph} - TS_{ph}$ holds. On the other hand, the internal energy is the sum of the ground state energy of the electronic system subject to the field of fixed nuclei (minimum of the energy within the Born-Oppenheimer approximation calculated by DFT), plus the zero point vibrational energy of the nuclei (calculated by DFPT taking into account the phonon dispersion of the system calculated at 0 K), plus a contribution of electrons at finite temperature which is usually negligible for insulators and semiconductors that is not taken into account. **Figure 5** shows the results of all quantities calculated between 0 and 800 K. Namely, Figure 5a–c show the difference of vibrational energy, Helmholtz free energy and entropy of $R\bar{3}m$ and $R3m$ phases with respect to the 2H structure. The phonon band structures of the 2H, $R\bar{3}m$ and $R3m$ phases modelled show no branches with negative (imaginary) frequencies along the selected path of the BZ, revealing that the three phases are mechanically stable (see Figure 4f). On the basis of DFT electronic energy calculations, the lowest energy phase turns out to be the $R3m$ GaS. Expressing the total energy per formula unit, namely one Ga atom plus one S atom, relative to the reference energy of the 2H phase, the $R3m$ phase has a negative value of 0.66 meV f. u^{-1}. This result shows the close proximity between these two configurations of GaS, rationalized by the difference in the weak interlayer coupling found between polytypes. Given the small energy differences, we tested several implemented schemes including vdW corrections in the exchange-correlation functional (truly non-local and semiempirical versions) and we obtained the same trend regarding total energy comparison. A systematic DFT study by Magorrian et al.[48], including many body dispersion corrections of the isostructural GaSe compound, also shows total energy differences on the sub-meV scale for the known $\beta -$, $\epsilon -$, $\delta -$ and $\gamma -$ polytypes, suggesting the sensibility of the final crystal structure to the growth conditions. Conversely, the phase $R\bar{3}m$ tuns out to have an energy of 10.54 meV f. u^{-1}. higher than the 2H phase. Figure 5d shows the free energy, including the contribution of the electronic degree of freedom to have $U_{el} + U_{ph} - TS_{ph}$. A crossing point of the curve corresponding to the $R3m$ phase through the zero at approximately 700 K (427 °C) can be clearly seen, indicating that at higher temperatures the 2H phase becomes thermodynamically favorable. Recently, the presence of a rhombohedral $\gamma -$ GaS phase was detected by XRD data on nanobelts samples synthetized by CVD at 600 °C,[49] indicating that growth conditions and/or geometric confinement can have an effect on phase. Furthermore, a new polymorph (labelled $\gamma' -$ GaSe) with the same space group $R\bar{3}m$ has been found in thin films grown by molecular beam epitaxy (MBE).[26] In Reference 26, the authors also found $R\bar{3}m$ GaSe to be a higher energy structure arguing that the layer-by-layer and out-of-equilibrium MBE growth conditions cause a 60° rotation of half of the TL around the central Ga—Ga bond giving rise to the centrosymmetric configuration. Additionally, first principles study by Zhou et al.[50] on single-TLs of 2H and $R\bar{3}m$ (labelled 1T when considering only one TL of the bulk crystal) GaS and GaSe predicts that the energy barrier between the two phases of 2H- and 3R- GaS and GaSe is much lower than in MoS_2, suggesting the possibility to grow one or the other phase depending on growth conditions. Moreover, their results show that doping could stabilize one phase over the other. Furthermore, considering the layered structure of the van der Waals GaS, we also need to consider that in the Van der Waals (vdW) epitaxy the interface between the substrate and the layers as well as the interaction between layers, is dominated by weak vdW bonds. According to this, it has been reported [51] that lattice mismatch as large as 50% in vdW epitaxy could be accommodated. This is further supported by the Raman spectra shown in Figure 5e,f for 2H and 3R GaS grown by CVD on crystalline (sapphire) and amorphous (glass) substrates. Independently of the substrate, the high frequency E Raman mode appears at 295 for the 2H and at 290 cm^{-1} 3R respectively, in agreement with the experimental and DFTP mode position calculations shown in Figure 4a, indicating that the substrate is not affecting the grown crystalline phase, consistently with van der Waals epitaxy. Noteworthy, it can be

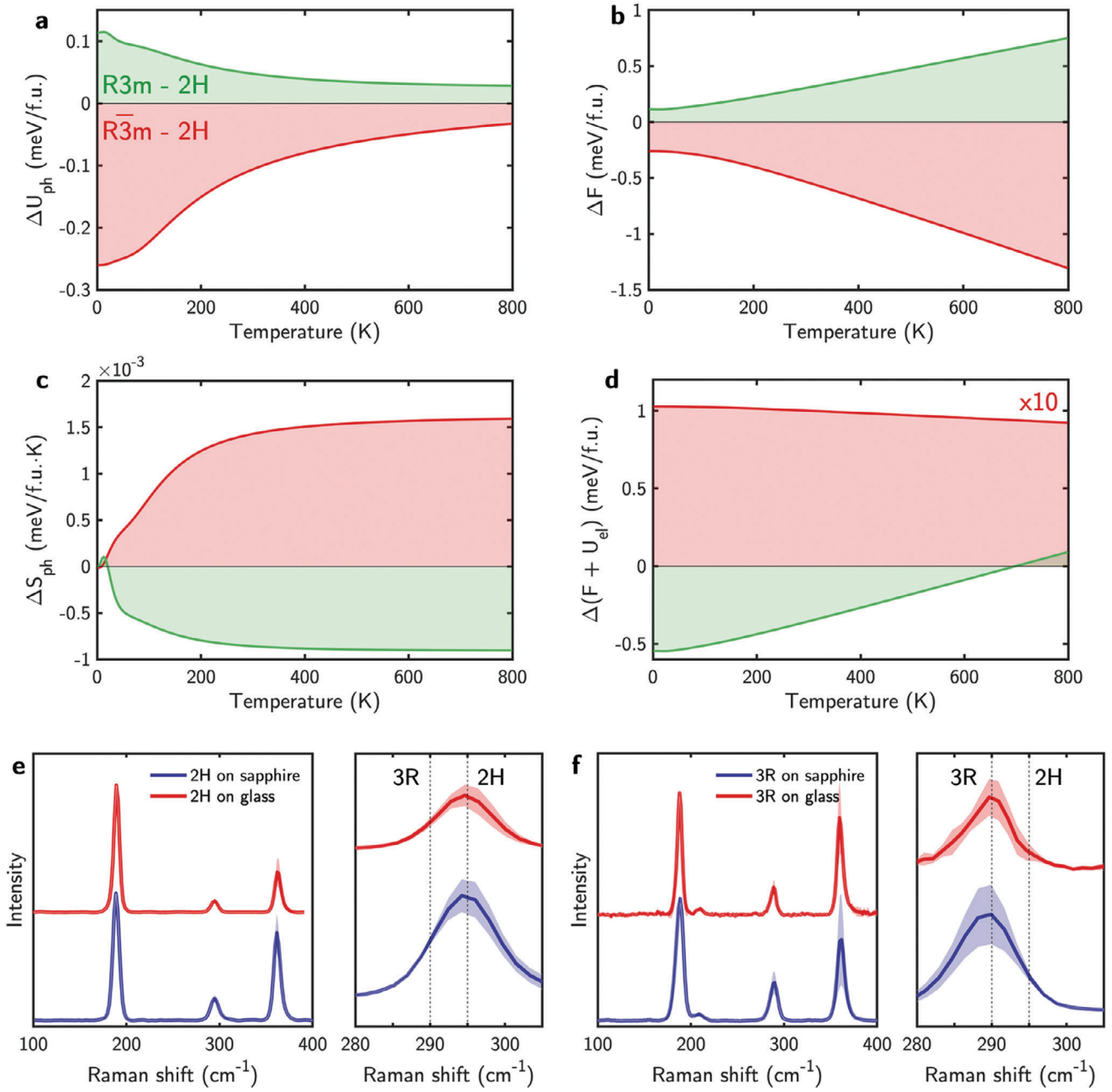

Figure 5. a) Vibrational energy variation ΔU_{ph}, b) Helmholtz free energy variation ΔF, c) entropy variation ΔS_{ph} and d) free energy variation $\Delta(F+U_{el})$ of *R3m* and *R$\bar{3}$m* with respect to the 2H phase as a function of the temperature per formula unit. Raman spectra and zoomed plot of experimentally measured high frequency E Raman mode in e) CVD 2H and f) CVD3R GaS grown on sapphire and glass substrates.

inferred that mainly growth conditions (determining a thermodynamic growth regime vs kinetic regime) affect the growth of the 3R- vs 2H phase. Indeed, an analysis of the various batches of grown GaS under various growth conditions supports that 3R-GaS can be grown at temperature below 600 °C and at high H_2 fluxes, whereas a growth temperature higher than 600 °C and low H_2 fluxes favors the 2H- phase.

Interestingly, although being reported to be a metastable phase at room temperature in agreement with our first principles thermodynamics calculations, the 3R phase synthetized by CVD has resulted to be stable over a year (from deposition) under ambient conditions. This is relevant for considering further applications of GaS as discussed in the next paragraph in light of its optical properties.

3.4. Electronic Structure and Optical Properties

Figure 6a shows the room temperature photoluminescence (PL) spectra of 2H and 3R GaS. It has been previously reported that

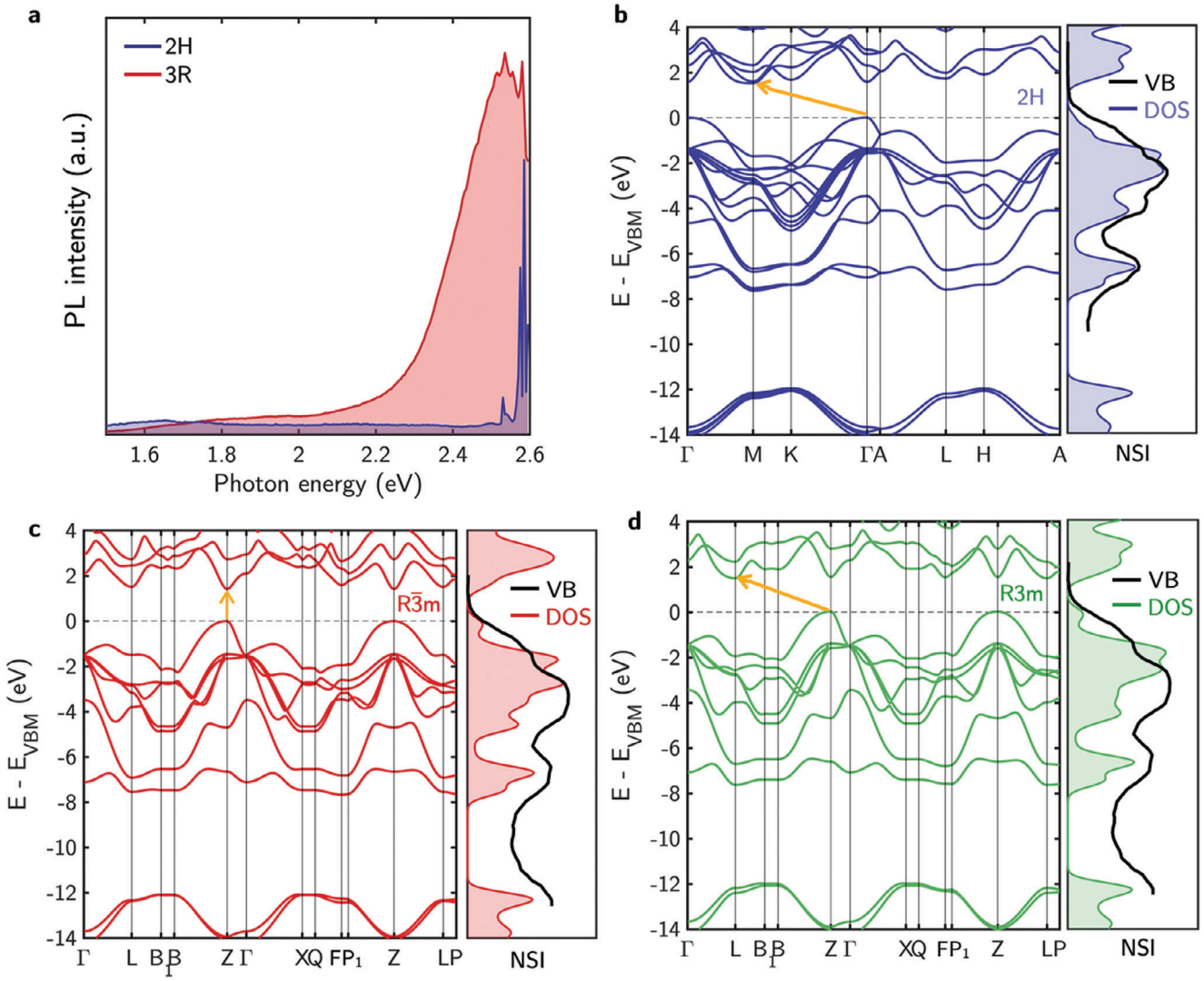

Figure 6. a) Photoluminescence spectra acquired for the 2H and 3R phases of GaS. Electronic band dispersion and density of states (DOS) calculated for the b) 2H, c) $R\bar{3}m$ and d) $R3m$ phase, respectively. Energies are plotted with respect to the VBM energy. The yellow arrows indicate the lowest energy gap in each case. With the DOS is plotted the XPS valence band.

the 2H phase of GaS is an indirect band gap semiconductor.[17] PL spectra acquired on the 2H sample corroborate this observation. The indirect nature of the lowest electronic excitation reduces the likelihood of radiative recombination processes, resulting in a flat photoluminescence spectrum as appreciated in Figure 6a. Conversely, a PL peak at ≈2.55 eV due to photogenerated electron-hole recombination through a radiative process can be seen for the 3R sample. This is a clear indication of a material with a direct band gap. This result is corroborated with theoretical calculations of the electronic structure of 2H, $R\bar{3}m$, and $R3m$ GaS phases at the generalized gradient approximation (GGA) level including vdW dispersion corrections. As can be seen in Figure 6b, the 2H phase shows an indirect band gap as previously reported. Similarly, the $R3m$ phase also shows an indirect optical band gap (Figure 6c). Finally, $R\bar{3}m$ GaS is predicted to have a direct band gap in accordance with the strong peak seen in the PL spectrum, as can be seen in Figure 6d. This is another hint towards confirming the $R\bar{3}m$ space group symmetry of our sample. Projection of the electronic levels onto the orbital degrees of freedom, not shown here, allows us to describe thoroughly the atomic-like features of the bands. For the three phases, the electronic band dispersion displays similar features, namely a manifold of bands below the valence band maximum (VBM) up to 8 eV mainly composed of S *3p* and Ga *4p* orbitals. Specifically, contributions from S $3p_z$ and Ga $4p_z$ plus *3s* are appreciable near the VBM, and between 6 and 8 eV there is a stronger contribution from Ga *4s* orbitals. Deeper bands in the range of 12 – 15 eV have a S *3s* and Ga *4d* character, the manifold of *d* bands of the metal are dispersionless as expected. Low energy conduction bands have mostly Ga *4s* and in plane $4p_{x/y}$ character, and a minor contribution from S *3s* and $3p_{x/y}$ levels. Figures 6b–d show clearly a series of valleys in the conduction levels with small energy differences. In the hexagonal 2H phase, the lower valleys appear at M, K and Γ points and the same structure is replicated on the BZ

edge points L, H and A. The VBM lies on Γand the conduction band minimum (CBM) on the M point. Rhombohedral $R\bar{3}m$ and $R3m$ phases share similar features, but the valleys appear on L, Z and F points due to the different crystal symmetry. The VBM in the $R3m$ phase lies on the Z point and the CBM on the L point respectively, giving an indirect band gap material. On the other hand, the direct band gap of the $R\bar{3}m$ phase opens across the Z point. The band gap of the 2H, $R\bar{3}m$, and $R3m$ phases come out to be 1.52 eV, 1.42 eV, and 1.47 eV respectively, calculated at the Kohn-Sham semi-local level. As a reference, the experimental forbidden gap of 2H GaS is ≈ 2.5 eV, evidently underestimated by our methodology. However, here we focus on the nature of the band gap and we can expect that this systematic error will not play a significant role in our comparison and analysis. To underpin this point, we mention that first theoretical calculations including higher levels of approximation like hybrid exchange-correlation functionals, and many body techniques corroborate the same trend. Additional to the band structure, the density of states (DOS) for each case are also shown in Figures 6b–d. The DOS are compared with valence band measurements performed by X-ray photoelectron spectroscopy (XPS) showing good agreement. Discrepancies near the valence edge can be attributed to changes in the electronic populations due to temperature effects not considered in the DFT calculations.

These findings shed new light on the potential applications and electronic properties of GaS thin films in various optoelectronic devices, considering the lack of 2D direct band gap semiconductors with energies close to 2.55 eV, apart from ZnSe and CdS (band gap at 2.60 eV and 2.42 eV, respectively).

4. Conclusion

We have demonstrated the growth of 3R GaS on sapphire substrates using chemical vapor deposition. The crystallographic analysis revealed that the films have a strong preferred *c*-axis orientation with low microstrain and moderate mosaicity. The combined approach of experimental X-ray diffraction, Raman and photoluminescence measurements with density functional theory calculations allowed us to determine that the 3R phase belongs to the space group $R\bar{3}m$ (no. 166). Through first principles calculations, we predict another polytype of the 2H phase, never reported experimentally, to be a competitive structure at low temperatures with symmetry $R3m$ (no. 160). We show that the 3R GaS phase is a direct band gap semiconductor with a band gap value of 2.55 eV (486 nm) and exhibits near-blue light emission at that photon energy, measured at room temperature. Together with ZnSe and CdS, this material represents one of the few direct band gap 2D semiconductors within the 2.4-2.6 eV range. Our findings pave the way to novel applications in optoelectronics, particularly in the development of efficient light-emitting devices such as LEDs or lasers, quantum dots, photodetectors, and crystalline-crystalline phase-change optical switches.

5. Experimental Section

2H GaS Single Crytal: Commercial bulk 2H GaS (2D semiconductors and HQ graphene) were mechanically exfoliated using the standard tape methods. Corning glass substrates were treated overnight in hydrogen peroxide and then cleaned with isopropyl alcohol, acetone, and ethanol.

CVD GaS Film: The GaS films were grown in a single-zone horizontal furnace on (0001) c-axis oriented sapphire and glass substrates. The reactor was pumped to a base pressure of 1.5×10^{-2} Torr and flushed with Ar gas to remove residual oxygen prior starting deposition. In the case of 3R GaS, high purity (99.99%) Ga_2S_3 powder was used as a single precursor heated to a reaction temperature of 800 °C in a 50 sccm H_2 flow and growth pressure of 100 mbar. The deposition temperature was set in the range of 550 to 600 °C. For the growth of 2H GaS, the Ga_2S_3 was heated to a reaction temperature of 800 °C in a 100 sccm H_2 flow resulting and growth pressure of 3 mbar. The deposition temperature was set in the range of 600 to 650 °C.

The thickness of the several investigated films, both 2H-GaS and 3R-GaS, was between few tens and several hundreds of nanometers. In this range, the authors have demonstrated already that there was no thickness dependence of the GaS properties, as already above 5 layers (corresponding ≈ to 5 nm) the properties converges to that of GaS bulk.

Characterization: The GaS films were structurally characterized with a combination of Raman spectroscopy and X-ray diffraction (XRD).

Raman spectroscopy was performed in backscattering configuration with a LabRam Horiba using a 532 nm wavelength laser (20 mW) with a ×100 microscope objective (NA = 0.9). Photoluminescence measurements were performed in the same Raman set up using a 470 nm wavelength laser (50 mW) with a ×100 microscope objective (NA = 0.9).

The XRD investigation was performed by reciprocal space maps (RSM). RSMs were obtained using a Panalytical Empyrean diffractometer equipped with a Cu X-ray tube and a Pix-Cel 2D detector with a 256 × 256 array sensor, covering a solid angle 3.3° × 3.3°. The reciprocal space along Q_x and Q_z was covered using $\omega/2\theta$ scans combined with azimuthal ϕ angle rotations. In order to initially identify reflections from GaS film, a full scan of reciprocal space available for the diffractometer with grazing incidence geometry ($Q_x > 0$) was performed by continuously spinning the sample in order to bring into diffraction condition reflections at different azimuthal angles. The identified Q_x and Q_z reflection positions were scanned over ϕ in order to evaluate how the reflections are distributed around the azimutal angle. Higher resolution scans of individual reflections were performed. Reciprocal lattice units (rlu) are defined here in nm^{-1} as $2\pi/d$, where d was the distance between crystallographic planes.

Morphological analysis was performed using atomic force microscopy (AFM) and scanning electron microscopy (SEM). AFM analysis was performed using the Autoprobe CP (Thermomicroscope). The sample topography and phase were recorded in a single-pass mode using a gold-coated Si tip (frequency of 80 Hz) in non-contact mode.

Scanning electron microscopy (SEM) was carried out with a Zeiss Supra 219 40 FEG SEM equipped with a Gemini field emission gun. Analyses were carried out at an extraction voltage of 3 kV and 221 a 30-µm aperture.

The elemental composition was evaluated by X-ray photoelectron spectroscopy (XPS). XPS analyses were performed by a Scanning XPS Microprobe (PHI 5000 Versa Probe II, Physical Electronics) equipped with a monochromatic Al Ka X-ray source (1486.6 eV), with a spot size of 200 mm. Survey (0–1200 eV) and high-resolution (HR) spectra (C1s, S2s, Ga3d) were acquired in FAT mode at a pass energy of 117.40 and 29.35 eV, respectively. Spectra were acquired at a take-off angle of 45° with respect to the sample surface. Surface charging was compensated using a dual beam charge neutralization system, and the hydrocarbon component of C1s spectrum was used as internal standard for charging correction, and it was fixed at 285.00 eV.

First Principles Calculations: Density functional theory (DFT) first principles calculations based on norm-conserving pseudopotentials (NCPP)[52] were carried out using the Quantum Espresso (QE)[47] code. Electronic exchange and correlation interaction was included at semi-local level with the generalized gradient approximation (GGA), using the exchange functional of Cooper[53] (C09x). To account for dispersion interactions, truly non-local correlations as given by Lee et al.[54] (vdW-DF2). Core electrons are described by ab-initio optimized Vanderbilt pseudopotentials, generated following the recipe given by Hamann[55] in the Kleinman–Bylander fully non-local separable representation,[56] available

in the PSEUDODOJO online database[57] (version 0.4.1 of the ONCVPSP code). NCPP for Ga and S used in the calculations that involve vdW non-local dispersion interactions were generated also with the ONCVPSP code available in the website http://www.mat-simresearch.com/. For Ga element, $3d^{10}4s^{2}4p^{1}$ were considered as valence electrons. Lighter chalcogenide S atom is constructed with an electronic configuration that includes six valence electrons ($3s^{2}3p^{4}$). Hexagonal (rhombohedral) 2H (3R) unit cell of GaS with 8 (4) atoms in total were employed through all the calculations. Brillouin zone integrations were carried out using a Monkhorst-Pack[58] sampling of 15 × 15 × 3 (12 × 12 × 12) points and an energy cutoff for plane waves expansion of 90 (90) Ry for the 2H (3R) phase to attain converged results. Geometric parameters reported were obtained by structural optimization, where atoms and unit cell parameters were allowed to relax until the maximum component of the force acting on any atom was smaller than 1.10^{-2} eV Å^{-1}, and the maximum component of the stress was 0.1 GPa. Vibrational modes and thermodynamic properties, within the harmonic oscillator approximation, were calculated with the THERMO_PW driver (https://dalcorso.github.io/thermo_pw/) using underlying QE routines based on density function perturbation theory (DFPT)[59] with the set of parameters aforementioned. A k-point mesh employed for phonon spectra was 10 × 10 × 2 (4 × 4 × 4) points for 2H (3R) GaS and a stringent threshold of forces up 5.10^{-5} eV Å^{-1} was set to yield converged phonon frequencies.

Acknowledgements

Y.G., D.J., and F.A. contributed equally to this work. The authors acknowledge the support from the European Union's Horizon 2020 research and innovation program (No 899598 – PHEMTRONICS). The National Research Council of Italy (CNR) was gratefully acknowledged for co-funding the acquisition at ICMATE-CNR of a XRD and a XPS systems in the frame of the "Roadmap per lo sviluppo delle infrastrutture e il Programma Biennale degli Interventi (delibera CdA 136/2020)". The authors also acknowledge computational resources and technical assistance from Scientific Computing Administration of the Johannes Kepler University (JKU), Linz, Austria and the Investigation Computational Service of Cantabria University (UC), Santander, Spain. Y.G. acknowledge founding from a Ramon y Cajal Fellowship (RYC2022-037828-I).

Conflict of Interest

The authors declare no conflict of interest.

Data Availability Statement

The data that support the findings of this study are available from the corresponding author upon reasonable request.

Keywords

2D materials, gallium sulfide, polymorphs, polytypes, post-transition metal chalcogenides

Received: November 24, 2023
Revised: March 2, 2024
Published online:

[1] M. Chhowalla, H. S. Shin, G. Eda, L.-J. Li, K. P. Loh, H. Zhang, *Nat. Chem.* **2013**, *5*, 263.
[2] D. Jariwala, V. K. Sangwan, L. J. Lauhon, T. J. Marks, M. C. Hersam, *ACS Nano* **2014**, *8*, 1102.
[3] M. Dai, C. Gao, Q. Nie, Q. Wang, Y. Lin, J. Chu, W. Li, *Adv. Mater. Technol.* **2022**, *7*, 2200321.
[4] M. S. Choi, B. Cheong, C. H. Ra, S. Lee, J.-H. Bae, S. Lee, G.-D. Lee, C.-W. Yang, J. Hone, W. J. Yoo, *Adv. Mater.* **2017**, *29*, 1703568.
[5] C. K. Y. Tan, W. Fu, K. P. Loh, *Chem. Rev.* **2023**, *123*, 8701.
[6] Y. Gutiérrez, S. Dicorato, A. P. Ovvyan, F. Brückerhoff-Plückelmann, J. Resl, M. M. Giangregorio, K. Hingerl, C. Cobet, M. Schiek, M. Duwe, P. H. Thiesen, W. H. P. Pernice, M. Losurdo, *Adv. Opt. Mater.* **2023**, *12*, 2301564.
[7] Y. Lu, J. Chen, T. Chen, Y. Shu, R. J. Chang, Y. Sheng, V. Shautsova, N. Mkhize, P. Holdway, H. Bhaskaran, J. H. Warner, *Adv. Mater.* **2020**, *32*, 1.
[8] A. Harvey, C. Backes, Z. Gholamvand, D. Hanlon, D. McAteer, H. C. Nerl, E. McGuire, A. Seral-Ascaso, Q. M. Ramasse, N. McEvoy, S. Winters, N. C. Berner, D. McCloskey, J. F. Donegan, G. S. Duesberg, V. Nicolosi, J. N. Coleman, *Chem. Mater.* **2015**, *27*, 3483.
[9] S. Lei, L. Ge, Z. Liu, S. Najmaei, G. Shi, G. You, J. Lou, R. Vajtai, P. M. Ajayan, *Nano Lett.* **2013**, *13*, 2777.
[10] P. Hu, Z. Wen, L. Wang, P. Tan, K. Xiao, *ACS Nano* **2012**, *6*, 5988.
[11] X. Zhou, J. Cheng, Y. Zhou, T. Cao, H. Hong, Z. Liao, S. Wu, H. Peng, K. Liu, D. Yu, *J. Am. Chem. Soc.* **2015**, *137*, 7994.
[12] C. H. Lee, S. Krishnamoorthy, D. J. O'Hara, M. R. Brenner, J. M. Johnson, J. S. Jamison, R. C. Myers, R. K. Kawakami, J. Hwang, S. Rajan, *J. Appl. Phys.* **2017**, *121*, 094302.
[13] J. Susoma, L. Karvonen, A. Säynätjoki, S. Mehravar, R. A. Norwood, N. Peyghambarian, K. Kieu, H. Lipsanen, J. Riikonen, *Appl. Phys. Lett.* **2016**, *108*, 073103.
[14] Z. Wang, M. Safdar, M. Mirza, K. Xu, Q. Wang, Y. Huang, F. Wang, X. Zhan, J. He, *Nanoscale* **2015**, *7*, 7252.
[15] E. Zallo, A. Pianetti, A. S. Prikhodko, S. Cecchi, Y. S. Zaytseva, A. Giuliani, M. Kremser, N. I. Borgardt, J. J. Finley, F. Arciprete, M. Palummo, O. Pulci, R. Calarco, *npj 2D Mater. Appl.* **2023**, *7*, 19.
[16] A. Chaves, J. G. Azadani, H. Alsalman, D. R. da Costa, R. Frisenda, A. J. Chaves, S. H. Song, Y. D. Kim, D. He, J. Zhou, A. Castellanos-Gomez, F. M. Peeters, Z. Liu, C. L. Hinkle, S.-H. Oh, P. D. Ye, S. J. Koester, Y. H. Lee, P. Avouris, X. Wang, T. Low, *npj 2D Mater. Appl.* **2020**, *4*, 29.
[17] Y. Gutiérrez, D. Juan, S. Dicorato, G. Santos, M. Duwe, P. H. Thiesen, M. M. Giangregorio, F. Palumbo, K. Hingerl, C. Cobet, P. García-Fernández, J. Junquera, F. Moreno, M. Losurdo, *Opt. Express* **2022**, *30*, 27609.
[18] Y. Lu, J. Chen, T. Chen, Y. Shu, R. Chang, Y. Sheng, V. Shautsova, N. Mkhize, P. Holdway, H. Bhaskaran, J. H. Warner, *Adv. Mater.* **2020**, *32*, 1906958.
[19] T. Chen, Y. Lu, Y. Sheng, Y. Shu, X. Li, R.-J. Chang, H. Bhaskaran, J. H. Warner, *ACS Appl. Mater. Interfaces* **2019**, *11*, 48172.
[20] W. Zhong, Y. Liu, X. Yang, C. Wang, W. Xin, Y. Li, W. Liu, H. Xu, *Mater. Des.* **2021**, *212*, 110233.
[21] S. Yang, Y. Li, X. Wang, N. Huo, J. B. Xia, S. S. Li, J. Li, *Nanoscale* **2014**, *6*, 2582.
[22] S. Dicorato, Y. Gutiérrez, M. M. Giangregorio, F. Palumbo, G. V Bianco, M. Losurdo, *Nanomaterials* **2022**, *12*, 465.
[23] S. Ahmed, P. K. Cheng, J. Qiao, W. Gao, A. M. Saleque, M. N. Al Subri Ivan, T. Wang, T. I. Alam, S. U. Hani, Z. L. Guo, S. F. Yu, Y. H. Tsang, *ACS Nano* **2022**, *16*, 12390.
[24] K. Allakhverdiev, F. Ismailov, L. Kador, M. Braun, *Solid State Commun.* **1997**, *104*, 1.
[25] M. I. Zappia, G. Bianca, S. Bellani, N. Curreli, Z. Sofer, M. Serri, L. Najafi, M. Piccinni, R. Oropesa-Nuñez, P. Marvan, V. Pellegrini, I. Kriegel, M. Prato, A. Cupolillo, F. Bonaccorso, *J. Phys. Chem. C* **2021**, *125*, 11857.
[26] J. Grzonka, M. S. Claro, A. Molina-Sánchez, S. Sadewasser, P. J. Ferreira, *Adv. Funct. Mater.* **2021**, *31*, 2104965.
[27] M. S. Sokolikova, C. Mattevi, *Chem. Soc. Rev.* **2020**, *49*, 3952.

[28] S. Chae, S. S. Chae, M. Choi, H. min Park, H. Chang, J.-O. Lee, T. Il Lee, *Nano Energy* **2019**, *56*, 65.
[29] Y.-C. Lin, D. O. Dumcenco, Y.-S. Huang, K. Suenaga, *Nat. Nanotechnol.* **2014**, *9*, 391.
[30] X. Gan, L. Y. S. Lee, K. Wong, T. W. Lo, K. H. Ho, D. Y. Lei, H. Zhao, *ACS Appl. Energy Mater.* **2018**, *1*, 4754.
[31] Y. Tan, F. Luo, M. Zhu, X. Xu, Y. Ye, B. Li, G. Wang, W. Luo, X. Zheng, N. Wu, Y. Yu, S. Qin, X.-A. Zhang, *Nanoscale* **2018**, *10*, 19964.
[32] M. Shiffa, B. T. Dewes, J. Bradford, N. D. Cottam, T. S. Cheng, C. J. Mellor, O. Makarovskiy, K. Rahman, J. N. O'Shea, P. H. Beton, S. V. Novikov, T. Ben, D. Gonzalez, J. Xie, L. Zhang, A. Patanè, *Small* **2023**, *20*, 2305865.
[33] M. S. Claro, J. P. Martínez-Pastor, A. Molina-Sánchez, K. El Hajraoui, J. Grzonka, H. P. Adl, D. Fuertes Marrón, P. J. Ferreira, O. Bondarchuk, S. Sadewasser, *Adv. Funct. Mater.* **2023**, *33*, 2211871.
[34] X. Wang, Y. Sheng, R.-J. Chang, J. K. Lee, Y. Zhou, S. Li, T. Chen, H. Huang, B. F. Porter, H. Bhaskaran, J. H. Warner, *ACS Omega* **2018**, *3*, 7897.
[35] M. P. Pardo, J. Flahaut, *Mater. Res. Bull.* **1987**, *22*, 323.
[36] K. R. Allakhverdiev, *Opt. Commun.* **1998**, *149*, 64.
[37] A. Kuhn, A. Chevy, R. Chevalier, *Acta Crysta.* **1976**, *32*, 983.
[38] M. Zhao, Z. Ye, R. Suzuki, Y. Ye, H. Zhu, J. Xiao, Y. Wang, Y. Iwasa, X. Zhang, *Light Sci. Appl.* **2016**, *5*, e16131.
[39] "HQ graphene Gallium sulfide," can be found under, https://www.hqgraphene.com/GaS.php (accessed: November 2023).
[40] P. F. Fewster, *X-Ray Scattering from Semiconductors and Other Materials*, World Scientific, Singapore **2015**.
[41] M. J. Taylor, *J. Raman Spectrosc.* **1973**, *1*, 355.
[42] J. P. van der Ziel, A. E. Meixner, H. M. Kasper, *Solid State Commun.* **1973**, *12*, 1213.
[43] J. C. Irwin, R. M. Hoff, B. P. Clayman, R. A. Bromley, *Solid State Commun.* **1973**, *13*, 1531.
[44] M. Hayek, O. Brafman, R. M. A. Lieth, *Phys. Rev. B* **1973**, *8*, 2772.
[45] Y. Guo, W. Zhang, H. Wu, J. Han, Y. Zhang, S. Lin, C. Liu, K. Xu, J. Qiao, W. Ji, Q. Chen, S. Gao, W. Zhang, X. Zhang, Y. Chai, *Sci. Adv.* **2018**, *4*, eaau6252.
[46] U. Argaman, R. E. Abutbul, Y. Golan, G. Makov, *Phys. Rev. B* **2019**, *100*, 054104.
[47] P. Giannozzi, S. Baroni, N. Bonini, M. Calandra, R. Car, C. Cavazzoni, D. Ceresoli, G. L. Chiarotti, M. Cococcioni, I. Dabo, A. D. Corso, S. de Gironcoli, S. Fabris, G. Fratesi, R. Gebauer, U. Gerstmann, C. Gougoussis, A. Kokalj, M. Lazzeri, L. Martin-Samos, N. Marzari, F. Mauri, R. Mazzarello, S. Paolini, A. Pasquarello, L. Paulatto, C. Sbraccia, S. Scandolo, G. Sclauzero, A. P. Seitsonen, et al., *J. Phys. Condens. Matter* **2009**, *21*, 395502.
[48] S. J. Magorrian, V. Zólyomi, N. D. Drummond, *Phys. Rev. B* **2021**, *103*, 094118.
[49] C. S. Jung, K. Park, F. Shojaei, J. Y. Oh, H. S. Im, J. A. Lee, D. M. Jang, J. Park, N. Myoung, C.-L. Lee, J. W. Lee, J. K. Song, H. S. Kang, *Chem. Mater.* **2016**, *28*, 5811.
[50] J. Zhou, H. L. Zhuang, *ChemistrySelect* **2016**, *1*, 5779.
[51] A. Koma, *J. Cryst. Growth* **1999**, *201*, 236.
[52] D. R. Hamann, M. Schlüter, C. Chiang, *Phys. Rev. Lett.* **1979**, *43*, 1494.
[53] V. R. Cooper, *Phys. Rev. B* **2010**, *81*, 161104.
[54] K. Lee, É. D. Murray, L. Kong, B. I. Lundqvist, D. C. Langreth, *Phys. Rev. B* **2010**, *82*, 081101.
[55] D. R. Hamann, *Phys. Rev. B* **2013**, *88*, 085117.
[56] L. Kleinman, D. M. Bylander, *Phys. Rev. Lett.* **1982**, *48*, 1425.
[57] M. J. van Setten, M. Giantomassi, E. Bousquet, M. J. Verstraete, D. R. Hamann, X. Gonze, G.-M. Rignanese, *Comput. Phys. Commun.* **2018**, *226*, 39.
[58] H. J. Monkhorst, J. D. Pack, *Phys. Rev. B* **1976**, *13*, 5188.
[59] S. Baroni, S. de Gironcoli, A. Dal Corso, P. Giannozzi, *Rev. Mod. Phys.* **2001**, *73*, 515.